Modeling and Analysis

GREENHOUSE GASES SCIENCE AND TECHNOLOGY

Deterioration of a fractured carbonate caprock exposed to CO_2-acidified brine flow

Brian Ellis and Catherine Peters, Princeton University, NJ, USA
Jeffrey Fitts, Brookhaven National Laboratory, Upton, NY, USA
Grant Bromhal, Dustin McIntyre, Robert Warzinski and Eilis Rosenbaum, US Department of Energy, National Energy Technology Laboratory, USA

Abstract: A flow-through experiment was performed to investigate evolution of a fractured carbonate caprock during flow of CO_2-acidified brine. A core was taken from the Amherstburg limestone, a caprock formation overlying the Bois Blanc and Bass Islands formations, which have been used to demonstrate CO_2 storage in the Michigan basin. The inlet brine was representative of deep saline brines saturated with CO_2, resulting in a starting pH of 4.4. Experimental conditions were 27 °C and 10 MPa. X-ray computed tomography and scanning electron microscopy were used to observe evolution of fracture geometry and to investigate mineralogical changes along the fracture surface. The initial brine flow corresponded to an average fluid velocity of 110 cm hr^{-1}. After one week, substantial mineral dissolution caused the average cross-sectional area of the fracture to increase from 0.09 cm^2 to 0.24 cm^2. This demonstrates that carbonate caprocks, if fractured, can erode quickly and may jeopardize sealing integrity when hydrodynamic conditions promote flow of CO_2-acidified brine. However, changes to fracture permeability due to mineral dissolution may be offset by unaltered constrictions along the flow path and by increases in surface roughness. In this experiment, preferential dissolution of calcite over dolomite led to uneven erosion of the fracture surface and an increase in roughness. In areas with clay minerals, calcite dissolution left behind a silicate mineral-rich microporous coating along the fracture wall. Thus, the evolution of fracture permeability will depend in a complex way on the carbonate content, as well as the heterogeneity of the minerals and their spatial patterning.

Keywords: caprock fracture; carbonate dissolution; CO_2 sequestration; fracture flow; leakage; risk assessment

Introduction

Secure geologic carbon sequestration requires a caprock that is able to contain CO_2 for long periods of time. Subsurface injection of large volumes of CO_2 may lead to conditions that generate new fractures in the caprock or reopen existing fractures.[1,2] Fractures, regardless of their origin, may serve as conduits for flow if they are hydraulically connected to an overlying aquifer.[3]

Correspondence to: Catherine A. Peters, Civil and Environmental Engineering Department, Princeton University, Princeton, NJ 08544, USA.
E-mail: cap@princeton.edu
Received May 8, 2011; revised June 13, 2011; accepted June 14, 2011
Published online at Wiley Online Library (wileyonlinelibrary.com). DOI: 10.1002/ghg.025

CO_2 that dissolves in water will acidify formation brines.[4] Carbonate minerals, such as calcite and dolomite, are known to be reactive when in contact with CO_2-acidified brines.[5] Therefore some degree of erosion is expected along flow paths where CO_2-acidified brine contacts carbonate rock, such as in hydraulically connected fractures in carbonate caprocks. Characterizing and modeling coupled fluid flow and reaction in fractures is challenging due to the interrelationship of these processes and the effects of spatial heterogeneities in fracture geometry and mineral distributions.[6–8] Reaction-induced changes in fracture geometry can alter intrinsic permeabilities and relative permeabilities in ways that are difficult to predict. It is well known that flow permeability increases with fracture aperture,[9] but flow is hindered with increasing roughness of fracture surfaces.[10,11] Furthermore, while mineral dissolution may enlarge the flow path, it is also possible that fracture permeability may decrease due to removal of the asperities holding the fracture open.[12] Finally, mineral dissolution may lead to clogging of the flow path caused by particle decohesion.[13] Therefore, predictions of long-term seal integrity require an understanding of how the complex interplay of CO_2-water-rock interactions and fluid transport will impact fracture evolution.

This paper presents results of an experimental study designed to investigate the micrometer- to centimeter-scale evolution of fracture geometry in an artificially fractured limestone caprock exposed to flow of CO_2-acidified brine. Experiments conducted at this scale are needed to determine the importance of complexities, such as mineral spatial heterogeneity, in controlling flow along fracture pathways. To investigate a relevant case, a caprock specimen was sampled from the drilling core of the injection well at one of the CO_2 injection demonstration sites of the US Department of Energy. The site is the Midwest Regional Carbon Sequestration Partnership's project located in Otsego County, Michigan. Approximately 60 000 tons of CO_2 were injected into the Bass Islands Dolostone between 2008 and 2009. This formation is overlain by the Bois Blanc formation, a cherty carbonate, and above that by the Amherstburg formation, a dense fossiliforous dolomitic limestone. The Amherstburg formation is considered the primary caprock for this injection site.[14] This is one of three existing deep-saline formation CO_2 injection projects that rely on a carbonate caprock as the primary seal for securing the injected CO_2.[15]

A seven-day core-flooding experiment was conducted in which CO_2-acidified brine flowed through an artificially fractured Amherstburg core sample. The brine composition was selected to represent a brine that has had time to react with the injection formation minerals under CO_2-saturated conditions prior to contact with the core. Temperature and pressure conditions were 27°C and 10 MPa. Under these conditions and at equilibrium with CO_2, the brine had a pH of 4.4. The evolution of fracture aperture was monitored in real-time using an X-ray computed tomography (CT) scanner. Before and after the experiment, 3-D reconstructions of the fracture geometry, aperture, and surface roughness were examined at higher resolution via micro X-ray CT (μCT). Finally, the cores were sectioned and examined with scanning electron microscopy (SEM). The combination of high resolution μCT and SEM analysis provides valuable insight into the mineralogy-dependent alterations of fracture geometry due to flow of reactive fluids.[13,16,17]

Methods

Sample characterization and brine composition

The Amherstburg sample used in this study came from a 10-cm diameter core that had been collected at a depth of 928 m during the drilling of the injection well at the Otsego County project site. A similar specimen from the Bois Blanc was also obtained, and used to estimate mineralogy of that formation. A 2.54-cm diameter vertical core was cut from the Amherstburg sample using a water-jet cutter to prevent unwanted mechanical degradation of the sample. The sample was artificially fractured prior to the experiment to enable flow. The fracture was induced under normal stress compression with dual knife-edge chisels perpendicular to the horizontal (XY) plane of the core. Prior to fracturing, the core was stabilized by coating the exterior with epoxy. This technique was successful in producing a fracture that propagated the length of the core. After the core was fractured, another coat of epoxy was applied to the core exterior, leaving only the ends exposed, to ensure the integrity of the epoxy coating and prevent lateral flow along the outer boundary during brine flow.

The Amherstburg caprock specimen is primarily composed of calcite and dolomite, in roughly equal proportions. Together, these minerals comprise >90%

Table 1. Inlet brine composition.

Species (total)	[mol L^{-1}]
Na^+	1.0×10^0
Cl^-	1.0×10^0
Ca^{2+}	6.4×10^{-3} to 3.5×10^{-2}
Mg^{2+}	1.8×10^{-2}
SO_4^{2-}	1.1×10^{-2}
$CO_{2(aq)}$	9.8×10^{-1}
pH	4.4 to 4.9

of the bulk sample, with the remaining rock containing a mixture of quartz, K-feldspar, clay minerals, and pyrite. The Bass Islands formation is predominately composed of dolomite with <10% other minerals including, in descending order of proportion, calcite, anhydrite, quartz, K-feldspar, and clay minerals. To determine these mineral compositions, X-ray diffraction was used to identify the primary minerals present. Then, a section of each sample was cut and polished for SEM analysis. Back-scattered electron (BSE) microscopy was used to differentiate mineral material from pore space, and where possible, differentiate between minerals. These BSE images were then combined with energy dispersive spectroscopy (EDS) elemental maps, such as those for calcium and magnesium. Specific minerals and their percent contribution to the sample area were identified using an algorithm that overlays the BSE gray-scale images with the EDS elemental maps. For example, the BSE images can be used to separate calcite from dolomite. Dolomite is assigned to regions of the EDS map where calcium and magnesium co-occur, with no other metals present, and where the BSE map has a gray-scale intensity corresponding to the range assigned to dolomite. These area estimates are used as a proxy for the percent volume contribution of each mineral and represent a semi-quantitative estimate of bulk mineralogy. Several 2-D images were taken at random locations on the polished section. The analysis of the BSE images builds upon the work of Peters.[18] The samples were examined at the Image Analysis Center at Princeton University using a Bruker X-ray diffractometer and a Quanta environmental scanning electron microscope.

The experimental brine composition shown in Table 1 was selected to represent CO_2-saturated brine that had already reacted with minerals in the injection formation. Specifically, the composition mimicked a CO_2-saturated 1 M NaCl brine reacted with dolomite, calcite, and anhydrite with saturation indices of approximately -2. Temperature and pressure conditions of 40°C and 10 MPa were chosen to represent those occurring at a depth of approximately 1 km, which is at the interface between the Amherstburg and the Bois Blanc formations. Brine pH and mineral saturation calculations were made using PHREEQC with the Pitzer.dat database.[19] Aqueous activity coefficients were estimated using the Pitzer model.[20] CO_2 solubility was estimated to be 0.98 mol L^{-1} following the work of Duan *et al.*[21] Thermodynamic constants shown in Table 2 were determined through the use of SUPCRT92 to account for system pressure and temperature conditions.[22]

Flow-through experiment

Figure 1 shows a simplified depiction of the experimental system that was constructed in the core-flow experimental facility at DOE NETL in Morgantown, WV. The fractured sample was placed in a rubber jacket that was inserted into a TEMCO triaxial carbon-fiber core holder. A confining pressure of 14 MPa was applied to the exterior of the rubber jacket to prevent lateral flow along the core exterior.

A batch of the synthetic brine was prepared in the brine reservoir by mixing deionized water and salts: NaCl (extra pure, Acros Organics), $CaCl_2$ (>96% pure, Acros Organics), $MgCl_2 \cdot 4H_2O$ (reagent grade ACS, Acros Organics), NaOH (>97% pure, Acros Organics), and Na_2SO_4 (>99% pure, Fisher). Then, two separate

Table 2. Thermodynamic constants (K) for acid-driven dissolution of calcite (Eqn 1) and dolomite (Eqn 2), and the solubility product constant (K_{sp}) for the dissolution of one mole of each mineral at 27 °C and 10 MPa. Saturation indices (SI) correspond to the solution conditions in the inlet brine. Reaction rate constants (k) are estimated following the work of Chou *et al.*[33] for ambient pressure, 25°C and pH = 4.4.

	log(K)	log(K_{sp})	SI	log(k) [mol m^{-2} s^{-1}]
Calcite	1.87	–8.39	–1.99	–4.1
Dolomite	2.54	–17.98	–2.29	–5.0

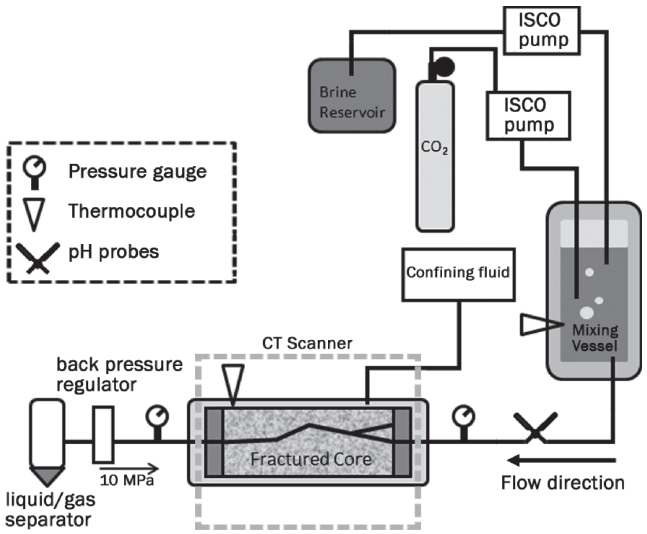

Figure 1. Simplified schematic of experimental design.

high-pressure syringe pumps (Teledyne Isco, Inc., Lincoln, NE, USA) delivered CO_2 (99.5% pure, Airgas) and brine to the high-pressure mixing vessel where they were allowed to equilibrate at 40°C and 10 MPa. The resulting CO_2 saturation in the brine was checked by comparing the measured pH to the predicted equilibrium pH. The measured pH values were within the expected range of model pH values shown in Table 1. Inlet brine samples were taken at the beginning of the experiment (higher calcium concentration, higher pH) and after three days (lower calcium concentration, lower pH). Precipitates, likely calcium-bearing, were visible in the brine reservoir early on in the experiment. As such, the day-3 composition is believed to be most representative of the fluid flowed through the fracture over the course of the experiment and is therefore used throughout this paper for the purpose of discussion. The pH measurements were made at system temperature and pressure conditions with use of high-pressure, high-temperature pH probes (Corr Instruments, LLC, San Antonio, TX, USA). Brine samples were treated with nitric acid and diluted before being analyzed via ICP-OES on a Perkin Elmer Optima 3000 XL.

To start the flow experiment, the CO_2 valve was closed and the brine pump was used to push the CO_2-saturated brine through the core. The experiment was designed to have a constant flow rate of 10 mL hr^{-1}, which was chosen such that the pumps would be refilled once every two days. This corresponded to an average initial fluid velocity of 110 cm hr^{-1}, which was calculated as the volumetric flow rate divided by the average initial cross-sectional area of the fracture. The system pressure was controlled at 10 MPa by a back-pressure regulator located near the outlet. Under the flow conditions of the experiment, there was no measureable pressure differential across the core and as such, there is no discussion of changes in core permeability presented in this paper. A temperature of 40 °C was successfully maintained in the mixing vessel; however, the average temperature measured at the core was 27 °C. This lower core temperature was due to safety limitations in heating of the core holder exterior coupled with heat losses along the upstream flow path and at the core-holder end caps.

X-ray computed tomography

Tomographic imaging of the core

X-ray computed tomography was used in two ways to perform non-destructive imaging of the fractured core before, during, and after the experiment. X-ray attenuation at beam energies greater than 100 keV corresponds to material density with a characteristic CT number that can distinguish mineral and void space.[23,24] The flow-through experiment was conducted within a Universal Systems HD-350E medical CT scanner. This allowed for real-time scans to be taken without disturbing the experiment. Scans were taken twice daily with a beam energy of 140 keV for the duration of the experiment providing information on fracture evolution. The medical scanner produces a series of 2-D slices with a voxel resolution of 250 μm in the plane of the slice and a thickness of 2 mm. This leads to data being averaged over the 2 mm depth of a single slice causing some blurring along areas where the fracture aperture changes within this length. It also means that a fracture aperture of less than 250 μm will only be positively identified as a void space due to a reduction in the CT number for the voxel that captures the fracture.

The fractured core was also imaged prior to and after completion of the experiment with a MicroXCT-400 scanner (Xradia, Inc., Pleasanton, CA, USA). The core was scanned dry and under ambient temperature and pressure conditions. Unlike the medical CT that scans a stationary sample while rotating the X-ray source and detector array, the μCT obtains a series of 2-D images with the sample rotating in a stepwise fashion between a stationary

source and detector. Xradia utilizes a proprietary arrangement of scintillators, optics, and high-resolution detector to achieve high-resolution, high-contrast X-ray images.[25] The large size of the core required that the sample be imaged in three sections of approximately 27 mm in length, allowing for some overlap between consecutive sections. The sample was scanned with an X-ray beam energy and power of 150 keV and 10 W, respectively, at rotational increments of 0.06° for the top section and 0.14° for the bottom two sections. The selected optics provided a 3-D reconstructed image with a voxel resolution of 27 μm, representing an order of magnitude improvement in resolution when compared to that achieved by the medical scanner.

Image analysis and aperture measurement

The medical CT scans were adjusted using the image processing Java application, ImageJ, in order to provide a uniform gray-scale image for the given range of CT numbers generated in the reconstruction. This also allowed for balancing of the contrast between consecutive scans, which then made it possible for cross-scan comparison of single 2-mm slices.

Two-dimensional slices of the reconstructed μCT scans were exported as jpeg files and ImageJ was again used to align and uniformly contrast these images. Each 2-D slice contained square pixels (27 μm × 27 μm) and represented a thickness (z-direction) of 27 μm. The field-of-view for these images was 27 × 27 mm, which is slightly larger than the core diameter. At these settings, the angle of the cone-beam of the μCT X-ray source introduces a wedge-shaped artefact at the top and bottom of the reconstructed images. This artefact can be seen at the top of Fig. 5(a), the bottom of which was cropped for this figure. If detailed whole-core information was required, more sections could have been scanned to provide sufficient overlap between sections to enable elimination of the wedge-shaped artefacts during stitching of the stacked sections. This was not necessary for the purposes of the research reported here. The three sections that were scanned of the 7.06-cm core still yielded ~6.5 cm (92%) of good μCT data for image analysis.

Prior to fracture aperture analysis, the fracture area of the entire set of 2-D images was isolated and the gray-scale contrast enhanced. The gray-scale images were then segmented using a thresholding algorithm in ImageJ based on a normalized histogram of the entire set of images. Fracture aperture was measured as the width of the fracture at every pixel column spanning the fracture. In areas where there were multiple fractures, a volumetric average was calculated to estimate an effective fracture aperture.

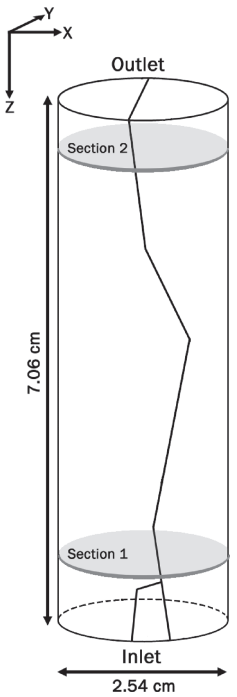

Figure 2. Diagram of fractured core with core dimensions and location of sections used for SEM analysis.

Sectioning and SEM imaging

To examine mineralogical alterations of the fracture surface, the core was sectioned and prepared for SEM imaging. After the experiment was finished and the core had been scanned, the core was dried and flooded with epoxy to allow for sectioning and further analysis with the SEM. To do this, the core was first flushed with ethanol and then dried via continuous flow of desiccated air. The core was flooded with epoxy with vacuum-assisted flow.

Figure 2 depicts the fracture orientation and identifies where samples were taken for SEM analysis. The core was sectioned along three planes. Section 1 was taken approximately 15 mm from the core inlet. Section 2 was taken approximately 8 mm from the outlet end of the core. The 15 mm section (core inlet to section 1) was then cut in the flow (Z) direction to

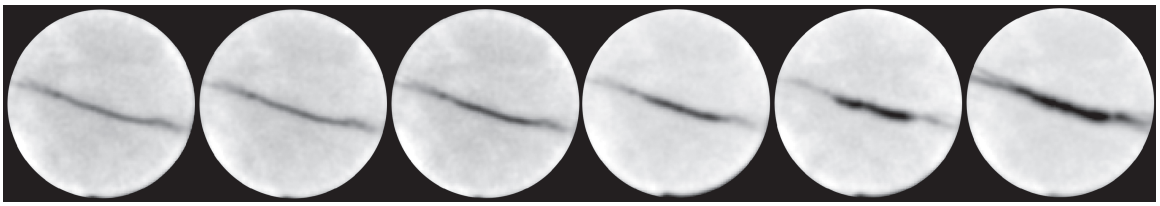

Figure 3. Six-day time series of medical CT scans of 2-mm section taken approximately 2 cm from core inlet. Scans from days 2 through 7 are shown, left to right. Consecutive scans are not precisely 24 hours apart, but show general progression of fracture erosion.

bisect the fracture perpendicular to its propagation in the XY plane. The sections were then polished and analyzed using the BSE/EDS image analysis technique previously described to identify the minerals adjacent to the fracture.

Results

Results from both the medical and μCT scans show evidence of an increase in fracture aperture throughout the core. Figure 3 shows a series of scans taken near section 1 with the medical CT scanner over the duration of the experiment. Even with the relatively low resolution of the medical CT images, an increase in fracture aperture is observed.

Figure 4 contains aperture maps for the fracture before (a) and after (b) flow of the CO_2-acidified brine. The difference in aperture is shown in Fig. 4(c). Figure 4(f) shows the average fracture aperture along the length of the core from the core inlet to the outlet. Initially, the fracture aperture was largest near the inlet with an average aperture of 480 μm and smallest near the outlet with an average aperture of 160 μm. The largest increase in aperture occurred in the one-third of the core near the outlet. This section of the core represents not only the area of largest absolute change in aperture but also the area with the largest average final aperture of 1100 μm. Figures 4(d) and 4(e) show the distribution of fracture apertures before and after flow, respectively. Initially, the median aperture of the fracture was 270 μm. The distribution of fracture apertures changed significantly after flow of the CO_2-acidified brine, resulting in a median aperture of 860 μm.

Along the 6.5 cm length, fracture void volume prior to flow of CO_2-acidified brine was ~0.6 ml and the average cross-sectional area was 0.09 cm^2. After seven days of exposure to the flowing CO_2-acidified brine, the fracture had a void volume of ~1.6 ml and average cross-sectional area of 0.24 cm^2. This represents an increase in flow area of ~2.7 times, resulting in a reduction in average flow velocity from 110 to 42 cm hr^{-1}, and a reduction in flushing from ~17 to ~6 fracture pore volumes hr^{-1}. In the field, a constant pressure gradient is more likely to exist, in which case the increase in flow area would increase the volumetric flow rate.

Close examination of the μCT images shows evidence that the fracture wall was eroding in a non-uniform manner. Figure 5 focuses on the one third of the core near the fluid inlet. Figure 5(a) shows the fracture after the experiment overlain with the initial fracture void shown in white. The μCT images show intermittent regions adjacent to the fracture void space that are slightly blurred. These are partially degraded zones. The zone highlighted by Box 1 in Fig. 5(a) is focused upon in Fig. 5(b), and is on the order of 300–400 μm in thickness. It appears to be of a fairly uniform thickness, suggesting that transport in this degraded zone may have been a limiting factor controlling the continued dissolution of the fracture surface.

The BSE and EDS analysis of sectioned segments of the core shed light on the mineralogical content of the fracture boundary and within the degraded zones observed in the μCT images. Along the fracture, calcite dissolved to a much greater extent than the other minerals present in the sample. The non-uniform degradation along the fracture wall is a result of the mineral spatial heterogeneity of the rock. Figures 6(a) and 6(c) show that the largest increases in fracture aperture occurred at points where calcite is in direct contact with the flowing brine. Figure 6(a) is the BSE image corresponding to Box 2 shown in

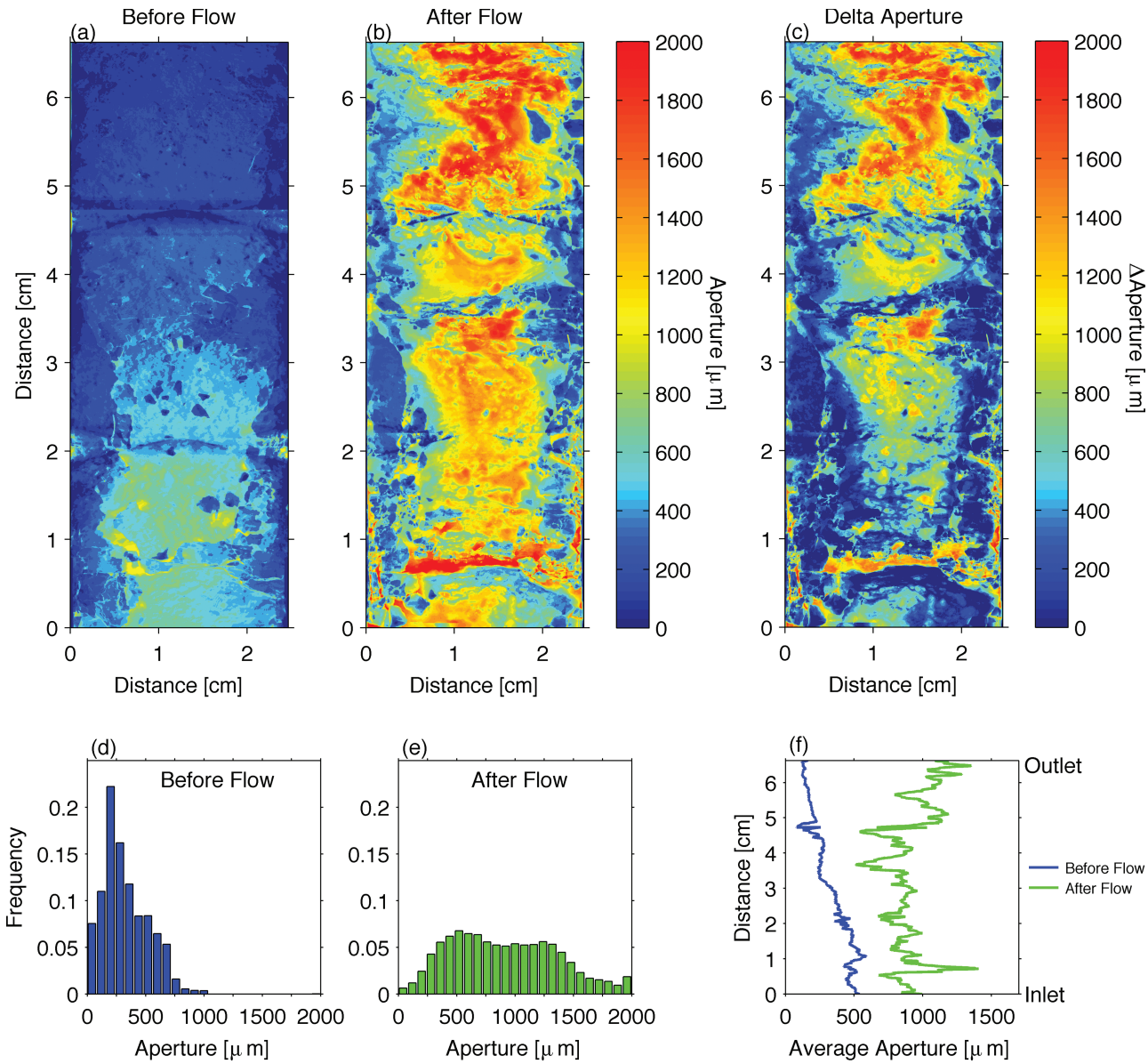

Figure 4. Fracture aperture maps of the fracture before (a) and after brine flow (b). The total change in aperture between the initial and final aperture measurements is shown in (c). Aperture width distributions are shown for the fracture before (d) and after brine flow (e). The average measured aperture along the length of the core is shown in (f).

Fig. 5(a). The smallest increases in fracture aperture correspond to areas where there are silicate minerals. In areas where calcite is intermixed with dolomite and other silicate minerals the dissolution of calcite leads to the formation of degraded zones along the fracture boundary as observed in the μCT images. Figure 6(b) provides a good example of preferential calcite dissolution in an area with homogenous mineral distribution. Figure 6(d), which is a close-up of the clay-rich zone in Fig. 6(c) highlighted within the box, demonstrates how calcite dissolution in an area of higher clay content can leave behind a continuous microporous silicate matrix.

The non-uniform change in average aperture along the length of the core, as shown in Fig. 4(f), is most consistent with an uneven distribution of calcite along the length of the core. Figure 6(c) is from section 2 (Fig. 2), which is the segment of the core that experienced the largest increase in aperture. Large grains of calcite are observed adjacent to the fracture wall.

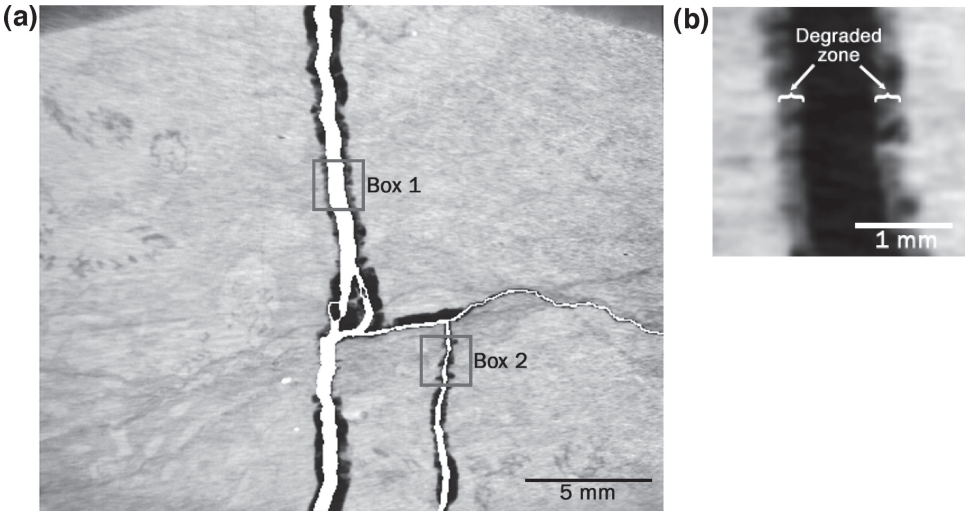

Figure 5. (a) μCT scan of 2-cm section near the core inlet after brine flow. The initial fracture void is shown in white overlying the fracture after dissolution to highlight the changes in fracture aperture. Box 1 in (a) is enlarged and shown in (b) to emphasize the development of a degraded zone along the fracture surface.

Here, there was erosion at a much faster rate than the surrounding rock of mixed calcite, dolomite, and clay mineral composition. There appears to be a distinct dissolution front along these calcite grains, which suggests the large increases in fracture aperture in this section are due to extensive dissolution and not grain plucking.

Discussion

The results of this experimental study demonstrate that for a carbonate caprock significant fracture erosion is possible when CO_2-acidified brine is able to flow continuously through the fracture. In the context of geologic carbon sequestration, this would increase the likelihood of leakage of CO_2 through the caprock, but predicting the extent and timeframe of this increased risk is complicated by how the fracture geometry evolves. In this discussion section, we put the findings from this experiment in context with comparable studies, and we use the collective findings of these studies to frame a discussion on how flow through caprock fractures may be influenced by geochemical alteration of fracture geometry. We also interpret the finding of the disproportionate dissolution rates of calcite and dolomite.

The rate and extent of geochemically driven evolution of caprock fractures will depend in a coupled way on fluid transport conditions (advective and diffusive mass transport), fluid composition (pH and mineral saturation conditions), caprock mineralogy (carbonates and silicates), and mineral spatial heterogeneity (mixed or banded). In this experiment, advective flow was dominant over diffusion. If mass transport in the fracture is diffusion-limited, then the erosion of the fracture surface will occur at a significantly reduced rate, as dissolution kinetics would be limited by the rate of diffusion of species away from reactive mineral surfaces. Diffusion of CO_2-acidified brines into the higher pH native fluids within the caprock may produce conditions that favor carbonate mineral precipitation, and thereby enhance the sealing capacity of the caprock.[26] In laboratory experiments involving reactive flow in fractured carbonate rocks, it was found that dissolution was favored in advection-dominated fractures and precipitation (of sulfates) was favored in diffusion-limited fractures.[27] Another relevant scenario is the coupled flow of acidified brine with advection- and buoyancy-driven flow of supercritical CO_2.[28] Andreani *et al.*[17] studied the impact of alternating brine and CO_2 gas flow through a fractured claystone caprock. They observed calcite dissolution during CO_2-acidifed brine flow and an increase in fracture aperture which was attributed to a cyclic process of clay decohesion during CO_2 gas flow followed by clay removal during subsequent brine flow. Upon further investigation of these results, Pèpe *et al.*[29] suggested that during CO_2 gas flow, the

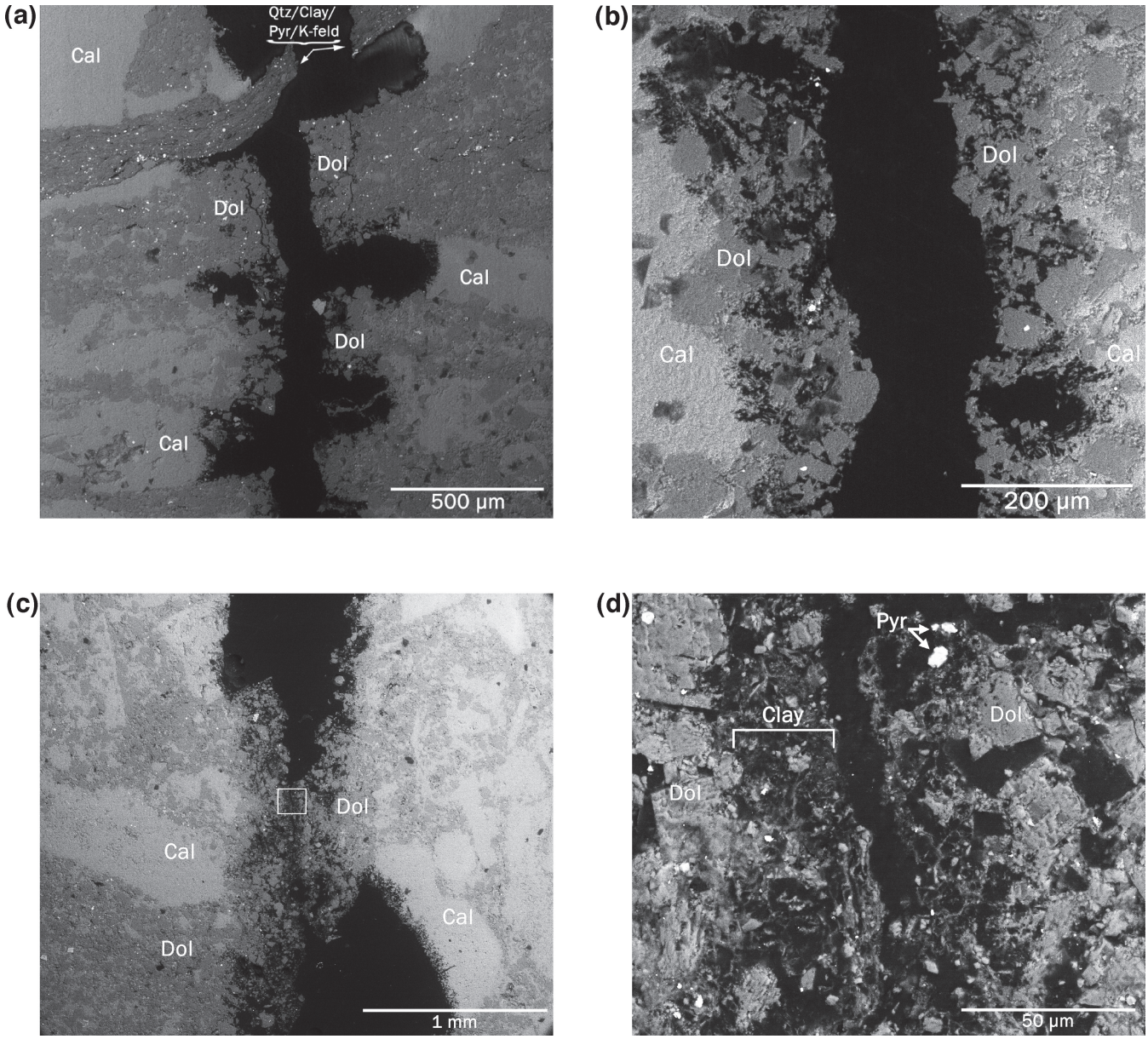

Figure 6. BSE images of (a) area highlighted by box 2 in Fig. 5(a) showing preferential dissolution of calcite leading to non-uniform aperture increases, (b) area of section 2 showing homogenous mineral distribution and development of degraded zone along fracture wall, (c) area of section 2 showing non-uniform aperture increases, and (d) close-up view of clay-rich microporous zone highlighted by box in Fig. 6(c).

interstitial fluids within the microporous clay matrix become highly acidified, leading to clay particle decohesion.

The evolution of caprock fractures will also depend strongly on the mineralogy of the caprock. In this study, there was substantial erosion of the fracture wall where there was calcite, and to a lesser but measurable extent where there was dolomite. The clay minerals, which are less reactive, remained, and possibly inhibited the dissolution of the carbonate minerals by slowing the transport of reaction products to the bulk brine phase. The slower rate of aperture growth in clay-rich regions of the fracture surface is particularly evident in Fig. 6(d). This implies that the presence of clay minerals may reduce the concomitant fracture aperture growth in a carbonate rock. This observation also suggests that weathered fracture surfaces, which can have significant clay

mineral deposits, may experience lower aperture growth rates relative to freshly created fracture surfaces. In a similar study, Noiriel *et al.*[13] investigated acidic water flow through an existing fracture in an argillaceous limestone, and reported that the preferential dissolution of calcite led to the development of a microporous clay coating along the fracture wall. Formation of the microporous clay coating was correlated with an increase in surface roughness, and an overall reduction in fracture permeability was primarily attributed to clay particle transport and accumulation within the fracture.

The mineralogical composition of the rocks used in the current study differed significantly from the rocks used in the studies by Noiriel *et al.*[13] and Andreani *et al.*[17] All three studies observed preferential dissolution of calcite within fractures of carbonate and carbonate-rich rocks; however, the clay mineral content of the three rock samples varied considerably. Noiriel *et al.*[13] used a limestone containing roughly 25% clay minerals, and Andreani *et al.*[17] used a carbonate-rich shale containing 45% clay minerals. The Amherstburg core used in the current study contained less than 10% non-carbonate minerals with an estimated clay mineral content of 2 to 5% of the bulk rock. The low percentage of clay minerals within the Amherstburg rock core, in addition to the fact that the fracture was fresh and not weathered, meant that the fracture surfaces would provide substantial contact with carbonate minerals.

Finally, the evolution of caprock fracture geometry is strongly dependent on the mineral spatial heterogeneity and configuration, as evidenced in Figs 6(a)–6(c), particularly as it relates to the fracture surfaces. The preferential dissolution of calcite, coupled with non-uniform mineral distribution along the fracture, led to increases in fracture surface roughness. This uneven fracture erosion is similar to that found by Gouze *et al.*[16] for a fractured limestone containing 15% dolomite. It is well known that fracture roughness can substantially reduce hydraulic flow through a fracture relative to what would be predicted from the average fracture aperture.[30] Additionally, the non-uniform dissolution of the fracture surface may lead to conditions that promote the development of preferential flow paths and possible wormhole formation along the fracture pathway.[31]

In this experiment, it was also observed that fracture aperture growth was negligible where the fracture intersected a silicate-rich band, as shown near the top of Fig. 6(a). The flow resistance through this unaltered silicate band may ultimately dominate the system flow, even though it is only a small portion of the total fracture geometry. According to the principles of critical path analysis in percolation theory, flow rate is largely dominated by the most resistive paths.[32]

In summary, for reactive flow through fractures in mineralogically heterogeneous rocks, the effect of increased fracture aperture may be offset by the effect of increased fracture roughness, and may even be negated if unaltered narrow restrictions remain.

In the remainder of the discussion section, we seek to explain the observed preferential dissolution of calcite over dolomite. Three factors are considered: mineral solubility, thermodynamic driving forces, and dissolution kinetics. The acid-driven mineral dissolution reactions for calcite and dolomite are, respectively,

$$CaCO_3(s) + H^+ \Leftrightarrow Ca^{2+} + HCO_3^- \quad (1)$$

$$CaMgCO_3(s) + 2H^+ \Leftrightarrow Ca^{2+} + Mg^{2+} + 2HCO_3^- \quad (2)$$

Table 2 contains the temperature- and pressure-adjusted equilibrium constants, K, for these reactions, along with the solubility product (K_{sp}) for the dissolution of one mole of each mineral. Although calcite is slightly more soluble than dolomite, the differences in solubility alone are unlikely to account for the observed preferential dissolution of calcite in this experiment. Values of the saturation index (SI), the logarithm of the ratio of the ion activity product to K, for each of the reactions shown above are given in Table 2. These minerals were at nearly equal saturation states, and in fact dolomite was slightly further from thermodynamic equilibrium. Thus thermodynamic forces were not the determining factor leading to preferential calcite dissolution.

The preferential dissolution of calcite over dolomite in these experiments is therefore attributed primarily to the differences in the reaction rate kinetics. Reaction rate constants for each mineral are also given in Table 2, based on literature-reported values for ambient pressure, 25 °C and pH=4.4.[33] The reaction rate constant for calcite dissolution is nearly one order of magnitude greater than that of dolomite, and therefore, dissolution kinetics was likely the primary driving force of the observed preferential calcite dissolution.

Conclusion

The experimental results from this study suggest that if hydraulically connected fractures exist in carbonate caprocks, flow of CO_2-acidified brine may lead to rapid dissolution along fracture pathways. The deterioration of the fracture in this experiment was due primarily to calcite dissolution and resulted in an increase in fracture cross-sectional area of ~2.7 times. This finding is not unexpected scientifically, but in the context of geologic sequestration of CO_2 it highlights the vulnerability of carbonate formations as caprocks for securing CO_2 underground, and it underscores the need to carefully evaluate their suitability during site selection. This study also demonstrates the complex manner in which fracture geometry can evolve under reactive flow conditions, making it difficult to predict the actual impact on fracture permeability. The differential dissolution rates of calcite and dolomite led to an uneven erosion of the fracture surface, which caused a substantial increase in surface roughness. The existence of unaltered silicate-rich bands along the fracture flow path and the increase in surface roughness may offset the effect of increases in average fracture aperture. This finding highlights the importance of understanding mineral spatial heterogeneity when trying to predict fracture evolution and ultimately, caprock seal integrity, when in contact with CO_2-acidified brine.

Because of the extreme degree and rate of fracture deterioration in this experiment, it is important to summarize the extent to which the scenario is plausible and representative. Several factors make this a plausible scenario including that the fractured specimen is from a real caprock from an actual CO_2 injection site, one that presumably satisfied numerous site selection criteria. In addition, the brine composition and experimental temperature and pressure conditions are representative of typical subsurface conditions. Finally, fractures in sedimentary rocks can exist, there is uncertainty in their detection, and fracture propagation can result from perturbations in fluid pressures, rapid expansions, and thermal gradients. The co-existence of several unique conditions also contributed to the observed rapid fracture deterioration. First, the carbonate caprock used contained only a small amount of non-carbonate minerals and was therefore quite susceptible to acid-driven dissolution. Second, the mineral surfaces along the fracture wall were not weathered since the fracture was fresh. Third, the brine was under-saturated with respect to calcium. Fourth, the flow rate may be high relative to what might occur in the field (although we have no basis for comparison). Therefore, this finding is representative of what could happen if several plausible events co-occurred.

Acknowledgements

The authors would like thank Dr William Harrison, III, (Michigan Basin Core Research Laboratory) for his help in obtaining the core samples used in this study, and Dr Hema Siriwardane (West Virginia University) for his help in fracturing the core. This project was supported through funding from the US Department of Energy National Energy Technology Laboratory, ORISE professional internship, ASCE Freeman Fellowship, US Department of Energy award number DE-FE0000749 and at Brookhaven National Lab under Contract No. DE-AC02-98CH10886. We also acknowledge the use of PRISM Imaging and Analysis Center which is supported in part by the NSF MRSEC program through the Princeton Center for Complex Materials (grant DMR-0819860). Finally, we acknowledge the perspectives and insights of the manuscript reviewers whose suggestions led to significant improvements in the presentation of this work.

References

1. Rutqvist J, Birkholzer JT and Chin-Fu Tsang, Coupled reservoir–geomechanical analysis of the potential for tensile and shear failure associated with CO_2 injection in multilayered reservoir–caprock systems. *Int J Rock Mech Min* **45**(2):132–143 (2008).

2. Shukla R, Ranjith P, Haque A and Choi H, A review of studies on CO_2 sequestration and caprock integrity. *Fuel* **89**:2651–2664 (2010).
3. Smith J, Durucan S, Korre A and Shi J, Carbon dioxide storage risk assessment: Analysis of caprock fracture network connectivity. *Int J Greenh Gas Con* **5**(2):226–240 (2011).
4. Ellis BR, Crandell LE and Peters CA, Limitations for brine acidification due to SO_2 co-injection in geologic carbon sequestration. *Int J Greenh Gas Cont* **4**(3):575–582 (2010).
5. Pokrovsky OS, Golubev SV, Schott J and Castillo A, Calcite, dolomite and magnesite dissolution kinetics in aqueous solutions at acid to circumneutral pH, 25 to 150°C and 1 to 55 atm pCO_2: New constraints on CO_2 sequestration in sedimentary basins. *Chem Geol* **265**:20–32 (2009).
6. Berkowitz B, Characterizing flow and transport in fractured geological media: A review. *Adv Water Resources* **25**(8–12):861–884 (2002).
7. Dijk PE, Berkowitz B and Yechieli Y, Measurement and analysis of dissolution patterns in rock fractures. *Water Resour Res* **38**(2):1013 (2002).
8. Detwiler RL, Experimental observations of deformation caused by mineral dissolution in variable-aperture fractures. *J Geophys Res* **113**:B08202 (2008).
9. Snow DT, Anisotropic Permeability of Fractured Media. *Water Resour Res* **5**(6):1273–1289 (1969).
10. Brown SR, Caprihan A, Hardy R. Experimental observation of fluid flow channels in a single fracture. *J Geophys Res* **103**(B3):5125–5132 (1998).
11. Crandall D, Bromhal G and Karpyn ZT, Numerical simulations examing the relationship between wall-roughness and fluid flow in rock fractures. *Int J Rock Mech Min* **47**(5):784–796 (2010).
12. Polak A, Elsworth D, Yasuhara H, Grader AS and Halleck PM, Permeability reduction of a natural fracture under net dissolution by hydrothermal fluids. *Geophys Res Lett* **30**(20):2020 (2003).
13. Noiriel C, Made B and Gouze P, Impact of coating development on the hydraulic and transport properties in argillaceous limestone fracture. *Water Resour Res* **43**:W09406 (2007).
14. Midwest Regional Carbon Sequestration Partnership (MRCSP). Factsheet for partnership field validation test. NETL Cooperative Agreement DE-FC26-05NT42589. September (2008).
15. Michael K, Golab A, Shulakova V, Ennis-King J, Allinson G, Sharma S and Aiken T, Geological storage of CO_2 in saline aquifers – A review of the experience from existing storage operations. *Int J Greenh Gas Con* **4**(4):659–667 (2010).
16. Gouze P, Noiriel C, Bruderer C and Loggia D, X-ray tomography of fracture surfaces during dissolution. *Geophys Res Lett* **30**(5):1267 (2003).
17. Andreani M, Gouze P, Luquot L and Jouanna P, Changes in seal capacity of fractured claystone caprocks induced by dissolved and gaseous CO_2 seepage. *Geophys Res Lett* **35**:L14404 (2008).
18. Peters CA, Accessibilities of reactive minerals in consolidated sedimentary rock: An imaging study of three sandstones. *Chem Geol* **265(**1–2):198–208 (2009).
19. Parkhurst DL and Appelo CAJ, *User's guide to PHREEQC (Version 2) – a computer program for speciation, batch-reaction, one-dimensional transport, and inverse geochemical calculations*. USGS Water-Resources Investigations Report. 99–4259, 312pp (1999).
20. Pitzer KS, Thermodynamics of electrolytes 1: Theoretical basis and general equations. *J Phys Chem* **77**:269–277 (1973).
21. Duan Z, Sun R, Zhu C and Chou I, An improved model for the calculation of CO_2 solubility in aqueous solutions containing Na^+, K^+, Ca^{2+}, Mg^{2+}, Cl^-, and SO_4^{2-}. *Marine Chem* **98**:131–139 (2006).
22. Johnson JW, Oelkers EH and Helgeson HC, SUPCRT92 – a software package for calculating the standard molal thermodynamic properties of minerals, gases, aqueous species, and reactions from 1 to 5000 bar and 0 to 1000 °C. *Comput Geosci* **18**:899–947 (1992).
23. Wildenschild D, Hopmans JW, Vaz CMP, Rivers ML, Rikard D and Christensen BSB, Using X-ray computed tomography in hydrology: systems, resolutions, and limitations. *J Hydrol* **267**:285–297 (2002).
24. Cai R, Lindquist BW, Um W and Jones KW, Tomographic analysis of reactive flow induced pore structure changes in column experiments. *Adv Water Resour* **32**:1396–1403 (2009).
25. Feser M, Gelb J, Chang H., Cui H, Duewer F, Lau SH, Tkachuk A and Yun W, Sub-micron resolution CT for failure analysis and process development. *Meas Sci Technol* **19**:094001, 8pp (2008).
26. Gherardi F, Xu T and Pruess K, Numerical modelling of self-limiting and self-enhancing caprock alteration induced by CO_2 storage in a depleted gas reservoir. *Chem Geol* **244**:103–129 (2007).
27. Singurindy O and Berkowitz B, The role of fractures on coupled dissolution and precipitation patterns in carbonate rocks. *Adv Water Resour* **28**(5):507–521 (2005).
28. Bryant SL, Lakshminarasimhan S and Pope GA, Buoyancy-dominated multiphase flow and its effect on geological sequestration of CO_2. *SPE J* **13**(4):447–454 (2008).
29. Pèpe G, Dweik J, Jouanna P, Gouze P, Andreani M and Luquot L, Atomic modelling of crystal/complex fluid/crystal contacts – Part II. Simulating AFM tests via the GenMol code for investigating the impact of CO_2 storage on kaolinite/brine/kaolinte adhesion. *J Crystal Growth* **312**:3308–3315 (2010).
30. Zimmerman RW and Bodvarsson GS, Hydraulic conductivity of rock fractures. *Transport Por Med* **23**(1):1–30 (1996).
31. Szymczak P and Ladd AJC, Wormhole formation in dissolving fractures. *J Geophys Res* **114**:B06203 (2009).
32. Berkowitz B and Balberg I, Percolation theory and its application to groundwater hydrology. *Water Resour Res* **29**(4):775–794 (1993).
33. Chou L, Garrels RM and Wollast R, Comparative study of the kinetics and mechanisms of dissolution of carbonate minerals. *Chem Geol* **78**:269–282 (1989).

Brian Ellis

Brian R. Ellis is a PhD candidate in Civil and Environmental Engineering at Princeton University. His research combines geochemical modeling and experimental work to investigate CO_2-water-rock interactions. He holds a Master's degree from Princeton University and Bachelor's degrees from the University of Michigan in Geosciences and Economics.

Catherine Peters

Dr Catherine A. Peters is a Professor of Environmental Engineering at Princeton University. She is an associated faculty member in the Department of Geosciences. Her expertise is in environmental geochemistry and engineering. She is a member of the Science Advisory Board Environmental Engineering Committee of the US EPA.

Dustin McIntyre

Dr Dustin L. McIntyre is a researcher at the National Energy Technology Laboratory in Morgantown, West Virginia, where he operates both a medical CT and an industrial CT scanner lab. His areas of expertise are in high-resolution CT scanning and the development of microwave and optically based ignition and diagnostic systems. He holds a PhD in mechanical engineering.

Jeffrey Fitts

Dr Jeffrey P. Fitts is a Geochemist in the Environmental Sciences Department at Brookhaven National Lab. His research focuses on physical and chemical interfacial processes in energy systems and waste management applications. He holds a PhD in Geochemistry.

Robert Warzinski

Robert P. Warzinski is a research chemist at the National Energy Technology Laboratory in Pittsburgh, PA, and is actively involved in carbon sequestration and methane hydrate research. He also utilizes microcomputed-tomography for investigating pore-scale phenomena in this research. He received his MSc in Chemistry from Duquesne University.

Grant Bromhal

Dr Grant S. Bromhal is the Research Group Leader of the Sequestration, Hydrocarbons, and Related Projects group in NETL's Geosciences Division. His research expertise includes the modeling of two-phase flow in porous media. He received his master's degree and PhD from Carnegie Mellon University in Civil and Environmental Engineering.

Eilis Rosenbaum

Eilis J. Rosenbaum is a research engineer with the National Energy Technology Laboratory. Most of her research has focused on gas hydrates and thermal properties. Currently she works with a micro CT scanner and visualizing and analyzing 3D data from the scanner. She obtained her MSc in Chemical Engineering from the University of Pittsburgh in 2004.

